A&A 508, 737–749 (2009)
DOI: 10.1051/0004-6361/200912774

Astronomy & Astrophysics

Deuterium chemistry in the Orion Bar PDR

"Warm" chemistry starring CH_2D^+ ⋆

B. Parise[1], S. Leurini[1,2], P. Schilke[1], E. Roueff[3], S. Thorwirth[1], and D. C. Lis[4]

[1] Max Planck Institut für Radioastronomie, Auf dem Hügel 69, 53121 Bonn, Germany
e-mail: bparise@mpifr-bonn.mpg.de
[2] European Southern Observatory, Karl-Schwarzschild-Str. 2, 85748 Garching bei München, Germany
[3] LUTH, Observatoire Paris-Meudon, 5 place Jules Janssen, 92195 Meudon Cedex, France
[4] California Institute of Technology, MC 301-17, Pasadena, CA 91125, USA

Received 26 June 2009 / Accepted 18 September 2009

ABSTRACT

Context. High levels of deuterium fractionation in gas-phase molecules are usually associated with cold regions, such as prestellar cores. Significant fractionation ratios are also observed in hot environments such as hot cores or hot corinos, where they are believed to be produced by the evaporation of the icy mantles surrounding dust grains, and are thus remnants of a previous cold (either gas-phase or grain surface) chemistry. The recent detection of DCN towards the Orion Bar, in a clump at a characteristic temperature of 70 K, has shown that high deuterium fractionation can also be detected in PDRs. The Orion Bar clumps thus appear to be a good environment for the observational study of deuterium fractionation in luke warm gas, allowing us to validate chemistry models for a different temperature range, where dominating fractionation processes are predicted to differ from those in cold gas (<20 K).
Aims. We aimed to study observationally in detail the chemistry at work in the Orion Bar PDR, to understand whether DCN is either produced by ice mantle evaporation or is the result of warm gas-phase chemistry, involving the CH_2D^+ precursor ion (which survives higher temperatures than the usual H_2D^+ precursor).
Methods. Using the APEX and the IRAM 30 m telescopes, we targeted selected deuterated species towards two clumps in the Orion Bar.
Results. We confirmed the detection of DCN and detected two new deuterated molecules (DCO^+ and HDCO) towards one clump in the Orion Bar PDR. Significant deuterium fractionations are found for HCN and H_2CO, but we measured a low fractionation in HCO^+. We also provide upper limits to other molecules relevant to deuterium chemistry.
Conclusions. We argue that grain evaporation in the clumps is unlikely to be a dominant process, and we find that the observed deuterium fractionation ratios are consistent with predictions of pure gas-phase chemistry models at warm temperatures ($T \sim 50$ K). We show evidence that warm deuterium chemistry driven by CH_2D^+ is at work in the clumps.

Key words. astrochemistry – line: identification – line: formation – ISM: abundances – ISM: individual objects: Orion Bar – ISM: molecules

1. Introduction

Despite the low deuterium abundance in the universe (D/H ~ 10^{-5}, Linsky 2003), high abundances of deuterated molecules have been observed in dark clouds and star-forming regions in the past few years, with detections of molecules containing up to three atoms of deuterium (ND_3: Lis et al. 2002; van der Tak et al. 2002, and CD_3OH: Parise et al. 2004), with noteworthy fractionation effects ($CD_3OH/CH_3OH \sim 1\%$, Parise et al. 2004).

Formation of those highly-deuterated molecules requires specific physical conditions, which makes them very interesting probes of the environments where they are observed. In molecular clouds, deuterium is mainly locked into molecular HD. Efficient transfer of deuterium from this reservoir at the low temperature of dark clouds must occur by means of ion-molecule reactions, and it has long been known that only a few ions react fast enough with HD to compete against electron recombination: H_3^+, CH_3^+ (Huntress 1977), and $C_2H_2^+$ (Herbst et al. 1987). The deuterated isotopologues of these three ions are thus considered to be the precursors of deuterium fractionation in the gas phase. The transfer of deuterium from the HD reservoir to other molecules is initiated by the following exothermic reactions:

$$H_3^+ + HD \rightarrow H_2D^+ + H_2 \quad (1)$$
$$CH_3^+ + HD \rightarrow CH_2D^+ + H_2 \quad (2)$$
$$C_2H_2^+ + HD \rightarrow C_2HD^+ + H_2. \quad (3)$$

The H_2D^+, CH_2D^+ and C_2HD^+ molecules then transfer their deuterium to the other species through ion-molecule reactions. Exothermicities are 232 K (Gerlich et al. 2002) for reaction (1), ~390 K (Asvany et al. 2004) for reaction (2), and ~550 K (Herbst et al. 1987) for reaction (3), so that the reverse reactions are inhibited at low temperatures. Efficient transfer of deuterium to molecules has been widely observed in cold regions where high levels of CO depletion are present, such as dark clouds or prestellar cores. In these environments, H_3^+ is predominantly responsible for the fractionation. Reaction (2) is understood to be predominant at slightly higher temperature ($T \sim 30$–50 K),

⋆ Based on observations with the IRAM 30 m telescope at Pico Veleta (Spain) and the Atacama Pathfinder EXperiment (APEX) telescope. IRAM is funded by the INSU/CNRS (France), the MPG (Germany) and the IGN (Spain). APEX is a collaboration between the Max-Planck-Institut für Radioastronomie, the European Southern Observatory, and the Onsala Space Observatory.

when (1) is no longer efficient because of the increased importance of its reverse reaction. Although the chemistry involving H_2D^+ is now basically understood, thanks to the numerous detections of H_2D^+ in prestellar cores (e.g., Caselli et al. 2003, 2008) and the parallel development of chemical models (e.g., Roberts et al. 2003; Walmsley et al. 2004; Flower et al. 2004; Pagani et al. 2009), the contribution of the CH_2D^+ chemistry has so far not been *observationally* investigated, because of the lack of observations targeting intermediate temperature sources that are warm enough so that the CH_2D^+ contribution becomes significant relative to H_2D^+, and cold enough for the chemistry not to be dominated by ice evaporation.

During an unbiased spectral survey of the Orion Bar using the APEX telescope, we detected a deuterated molecule (DCN) for the first time in a molecular clump in a Photon-Dominated Region (hereafter PDR, Leurini et al. 2006). This was however unexpected due to the high temperature ($T \sim 70$ K) that is characteristic of this clump. The fractionation ratio deduced from these observations is 0.7%, a value intermediate between the one observed in dark clouds (L134, 5%, Turner 2001) and hot cores (Orion, 0.1%, Schilke et al. 1992; a sample of hot cores, 0.1−0.4%, Hatchell et al. 1998).

DCO^+ was not detected in this survey, with an upper limit on the DCO^+/HCO^+ ratio of ∼0.1% (see below), although observations in other environments infer similar fractionation ratios for the two species (dark cloud L134: Tiné et al. 2000; Turner 2001; low-mass protostar IRAS16293: van Dishoeck et al. 1995). We proposed that this may be an indication that chemistry involving CH_2D^+ as the precursor for deuterium transfer to molecules is at work in the Orion Bar, making it a reference environment for the study in further detail of reactions involving these routes. This possibility was confirmed by the theoretical modelling study of Roueff et al. (2007). Since the DCN detection by Leurini et al. (2006), DCO^+ was detected towards the Horsehead PDR (Pety et al. 2007), in a cold (10−20 K) condensation shielded from the UV illumination. The observations we present in this paper are targetting warmer regions than the condensation observed by Pety et al. (2007).

We present here a detailed investigation of the deuterium chemistry at work in the dense clumps in the Orion Bar, based on observations with the APEX and IRAM 30 m telescopes. Observations are described in Sect. 2, the physical conditions in the clumps (temperature and H_2 densities) are derived in Sect. 3, the relative abundances and fractionations of targeted molecules are determined in Sect. 4, and the chemistry is discussed in Sect. 5.

2. Observations

The Orion Bar, located in the Orion A molecular cloud, is a well studied PDR, mostly because of its nearly edge-on morphology. Its distance is estimated to be 414 pc (Menten et al. 2007). It is illuminated by the young Trapezium stars, located some 2′ to the north-west. Previous studies have shown that this PDR has a clumpy structure (see Sect. 3). The interferometric observations of Lis & Schilke (2003) displayed a series of molecular clumps, as traced by the $H^{13}CN(1-0)$ transition, located in the cloud some 10″ behind the H/H_2 transition. In the present study, we use the nomenclature defined by Lis & Schilke (2003) to refer to the clumps.

We present the APEX and IRAM 30 m observations of the Orion Bar, which targeted in particular clump 1 and 3 of Lis & Schilke (2003). Unless otherwise stated, the transition frequencies of the molecules are taken from the Cologne Database for Molecular Spectroscopy (Müller et al. 2001; Müller et al. 2005). Table 1 summarizes the observations presented in this paper.

Table 1. Summary of the observations.

Transition	Frequency (GHz)	Telescope	Beamsize	Targetted clump
DCN(2–1)	144.8280015	IRAM 30 m	17″	1, 3
DCN(3–2)	217.2385378	IRAM 30 m	11″	1, 3
DCN(4–3)	289.6449170	APEX	21″	map
DCN(5–4)	362.0457535	APEX	17″	1, 3
DCO^+(2–1)	144.0772890	IRAM 30 m	17″	1, 3
$HDCO(2_{11}–1_{10})$	134.2848300	IRAM 30 m	18″	3
CH_2DOH(2–1)	89.3 (band)	IRAM 30 m	28″	1, 3
$HDO(2_{1,1}–2_{1,2})$	241.5615500[1]	IRAM 30 m	10″	3
C_2D(2–1)	144.3 (band)	IRAM 30 m	17″	3
DNC(2–1)	152.609774	IRAM 30 m	16″	3
$H^{13}CN$(1–0)	86.3399215	IRAM 30 m	28″	1, 3
$H^{13}CN$(3–2)	259.0117978	IRAM 30 m	9.5″	1, 3
$H^{13}CN$(4–3)	345.3397694	APEX	18″	map
$H^{13}CO^+$(1–0)	86.7542884	IRAM 30 m	28″	1, 3
HCO^+(1–0)	89.1884957	IRAM 30 m	28″	1, 3
$H_2^{13}CO(2_{11}–1_{10})$	146.6356717	IRAM 30 m	17″	3
$C^{17}O$(1–0)	112.36	IRAM 30 m	22″	3
$C^{17}O$(2–1)	224.71	IRAM 30 m	11″	3
$CH_3OH(5–4)$[2]	241.8 (band)	IRAM 30 m	10″	map
CH_3OH(6–5)	290.1 (band)	APEX	21″	1, 3
$CH_3OH(1_1–1_0$ A)	303.367	APEX	21″	1, 3
HNC(4–3)	362.63	APEX	17″	1, 3

[1] JPL database.
[2] HERA observations (see Leurini et al. (submitted) for more detail).

2.1. APEX observations

Using the APEX telescope on Chajnantor (Chile), we mapped the Orion Bar in the DCN(4–3) and $H^{13}CN$(4–3) transitions. The double-sideband APEX2a receiver (Risacher et al. 2006) was tuned to 289.0000 GHz (DCN) and 345.3397 GHz ($H^{13}CN$), and connected to the two units of the FFTS backend (Klein et al. 2006), each with 8192 channels, leading to a velocity resolution of 0.13 and 0.11 km s^{-1}, respectively, over twice the 1 GHz bandwidth. The APEX beamsize is 21″ (respectively 18″) at 289 GHz (respectively 345 GHz).

The (0″, 0″) position of the map is $\alpha(2000) = 05^h35^m25.3^s$, $\delta(2000) = -05°24'34.0''$, corresponding to the "Orion Bar (HCN)" position of Schilke et al. (2001), the most massive clump seen in $H^{13}CN$ (Lis & Schilke 2003), as well as the target of the spectral survey of Leurini et al. (2006). The maps were obtained using the on-the-fly mode, with a dump every 6″. The reference position was taken to be at the (600″, 0″) offset position from the center of the map.

The observations were performed between July 19th and August 2nd, 2006, in very good to good weather conditions (with a precipitable water vapor ranging from 0.3 to 1.5 mm). The typical DSB system temperatures were 115 and 200 K at 289 and 345 GHz, respectively. Several CH_3OH(6–5) transitions were also present in the DCN(4–3) setup. DCN(5–4) and HNC(4–3) were observed towards the two clumps on June 28th, 2007, with T_{sys} around 200 K.

Observed intensities were converted to T_{mb} using $T_{mb} = T_a^*/\eta_{mb}$ where $\eta_{mb} = 0.73$ (Güsten et al. 2006). We focus here on the observations towards clumps 1 and 3, and

analyze the spatial distribution across the Bar in a later paper (Parise et al. in prep.).

2.2. IRAM 30 m observations

We targeted the Orion Bar during three observing runs at the IRAM 30 m telescope. During the first run, we used the ABCD receivers, targeting only the two clumps in the Bar. The second run consisted of mapping the Bar with the HERA receiver. Some complementary data on the two clumps were also acquired as part of a third run.

2.2.1. Single pixel receivers

Using the IRAM 30 m telescope, we observed different species toward the two brightest $H^{13}CN$ clumps of the Orion Bar – "clump 1" at offset position (0″, 0″) and "clump 3" at position (−50″, −40″), as denoted by Lis & Schilke (2003). Besides observing different transitions of DCN to constrain the excitation, and looking for a lower excitation line of DCO^+ than the one that was not detected with APEX, we selected for our search molecules that can be synthesized in the gas phase via channels involving the CH_2D^+ ion. These molecules include HDCO and C_2D (Turner 2001). We also searched for CH_2DOH and HDO, to constrain any possible ice chemistry contribution.

The observations were performed from September 29th to October 7th, 2006, in variable weather conditions. Four receivers were used simultaneously to observe two different frequency bands (either in the AB or CD setup). The observed lines are listed in Table 1. The receivers were connected to the VESPA correlator in parallel mode, leading to different velocity resolutions depending on the transition. Additionally, the Bonn Fourier Transform Spectrometer (Klein et al. 2006) was connected to two of the receivers, providing a 850 MHz bandwidth.

Some additional data (DCN(3−2) as well as integration on CH_2DOH towards both clumps) were taken during a third observing run in May 2008, in poor (CH_2DOH data) to moderate (DCN data) weather conditions.

2.2.2. HERA observations

The Orion Bar was mapped in selected methanol and formaldehyde transitions using the HERA receiver, a heterodyne array consisting of two arrays of 3×3 pixels with 24″ spacing. The observations were performed during the winter 2007 HERA pool observing period. The full dataset is presented in Leurini et al. (2009). Here we analyze the methanol observations towards the two clumps to derive their physical properties.

All intensities of observations from the IRAM 30 m telescope were converted to $T_{\rm mb}$ using $T_{\rm mb} = \frac{F_{\rm eff}}{B_{\rm eff}} T_{\rm a}^*$, where $B_{\rm eff}$ is the main beam efficiency and $F_{\rm eff}$ is the forward efficiency. The main beam efficiencies decrease from 78% to 50% between 87 and 241 GHz[1]. Forward efficiency is 95% at 3 mm, 93% at 2 mm, and 91% at 1.3 mm.

3. The clumpy morphology of the Orion Bar

The Orion Bar was shown to have an heterogeneous structure, with clumpy molecular cores embedded in an interclump gas. The two-component morphology was first inferred by Hogerheijde et al. (1995) and Jansen et al. (1995), because single-dish observations of CS, H_2CO, and HCO^+ could not be described by a single density component. The clumpy structure was later confirmed directly by interferometric observations (Young Owl et al. 2000). The clumps have a density of several 10^6 cm^{-3}, while the density of the interclump gas is ∼10^4–10^5 cm^{-3} (Young Owl et al. 2000). Interferometric maps demonstrated that $H^{13}CN$ is confined mostly to the clumps (Lis & Schilke 2003), which are relatively cold (∼70 K) compared to the interclump gas (of a typical temperature of 150 K).

In the following, we discuss the physical parameters of the clumps, based on new observations. We first derive the H_2 column density (Sect. 3.1), and then the temperature and H_2 density based on methanol observations (Sect. 3.2).

3.1. The H_2 column density of the clumps

We attempt to derive the H_2 column density in the two clumps as accurately as possible, to be able to compute molecular abundances relative to H_2 in the following sections. This will then allow us to compare the measured fractional abundances to predictions of chemical models.

3.1.1. Clump 1

An H_2 column density of 9×10^{22} cm^{-2} averaged on the 18″ beam was derived towards clump 1 by Leurini et al. (2006) from analysis of the $C^{17}O$(3−2) emission line, assuming a rotational temperature of 70 K.

We can also estimate the H_2 column density in the clump by analyzing the dust emission observed in the frame of a project targeting clump 1 with the Plateau de Bure interferometer in March, April, and December 2004 (follow-up project of the work from Lis & Schilke 2003). The observations were performed in the mosaic mode, with seven fields covering clump 1 in a hexagonal pattern with a central field. The 3 mm receivers were tuned to the ^{13}CO(1−0) frequency (110 GHz), and the 1 mm receivers targeted H_2CO at 218 GHz. The array configurations, UV coverage and 1 mm observations are discussed in detail in Leurini et al. (2009). The receiver temperatures at 3 mm were around 200 K or lower.

Although continuum emission from clump 1 is not detected at 1 mm, weak emission is detected at 3 mm. This suggests that the density profile of the clump is rather smooth, and that its emission is mostly filtered out by the interferometer at 1 mm. The integrated intensity measured in a 10″ diameter aperture centered on the clump is 0.043 Jy, and 0.12 Jy in a 20″ diameter aperture. Assuming $T_{\rm dust}$ = 45 K (see Sect. 3.2), $\beta = 2$ and $\kappa_{230\,\rm GHz} = 3.09 \times 10^{-1}$ cm^2 g^{-1} (Ossenkopf & Henning 1994), we derive $N_{\rm H_2} = 1.6 \times 10^{23}$ cm^{-2} (resp 1.1×10^{23} cm^{-2}) averaged in a 10″ (resp 20″) area centered on the clump. These values are intermediate and consistent within a factor of 2 both with the column densities derived by Leurini et al. (2006), and by Lis & Schilke (2003) from $H^{13}CN$ observations (2.6×10^{23} cm^{-2}). In the following, we use our newly derived value $N_{\rm H_2} = 1.6 \times 10^{23}$ cm^{-2}.

3.1.2. Clump 3

Clump 3 was not targeted by the Plateau de Bure observations presented in Sect. 3.1.1. No continuum was detected either at 3 mm in the study of Lis & Schilke (2003), which implies that the density profile of the clump may again be rather smooth. From

[1] See http://www.iram.es/IRAMES/telescope/telescopeSummary/telescope_summary.html.

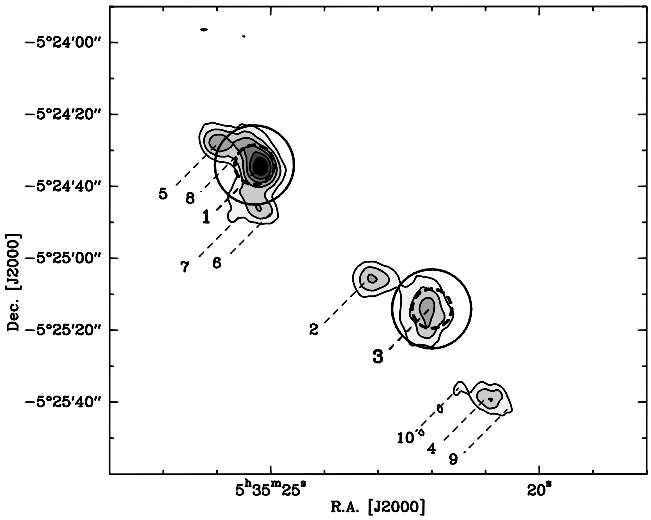

Fig. 1. In grey scale, the $H^{13}CN$ (1–0) transition observed with the Plateau de Bure interferometers by Lis & Schilke (2003). The numbers indicate the clumps identified by the same authors. The solid and dashed circles outline the beams of the APEX (~290 GHz) and IRAM 30 m (~241 GHz) telescopes, respectively.

the $H^{13}CN$ observations of Lis & Schilke (2003), the H_2 column density is measured to be 1.9×10^{23} cm^{-2}.

Using the IRAM 30 m telescope, we targeted the 1–0 and 2–1 transitions of $C^{17}O$ towards this clump. The hyperfine structure of the 1–0 transition is clearly resolved. The two observed lines have a rotation temperature of 12 K, and lead to a $N_{H_2} = 8 \times 10^{22}$ cm^{-2}, averaged over the extent of the clump (8″, see below).

In the following, we therefore assume an intermediate value of column density between those measured from $H^{13}CN$ and $C^{17}O$, $N_{H_2} = 1.3 \times 10^{23}$ cm^{-2}, averaged across the 8″ clump.

3.2. Physical conditions in the clumps : CH_3OH analysis

To determine the properties of the gas in the clumps, we analysed the methanol emission at 241 and 290 GHz. The beam of the APEX telescope at 290 GHz is almost twice as large as that of the IRAM antenna, and therefore samples different gas volumes (see Fig. 1). We therefore smoothed the HERA data to the resolution of the APEX telescope at 290 GHz. For the analysis, we used the technique described by Leurini et al. (2004) for the study of multi-line CH_3OH observations, which consists of modelling all the lines simultaneously with a synthetic spectrum computed using the large velocity gradient approximation, and comparing it to the observations. Rest frequencies are taken from Xu & Lovas (1997), while the collisional rates were computed by Pottage et al. (2002, 2004). The parameters defining the synthetic spectrum are: source size, kinetic temperature, column density, velocity width, and velocity offset (from the systematic velocity of the object). The line width and the velocity of the object are not free parameters, but are given as input values to the model. Finally, several velocity components, which are supposed to be non-interacting, can be introduced.

For our analysis, we modelled the emission towards each clump with a single component model, and neglected effects due to infrared pumping. As free parameters, we used the column density of the two symmetry states of methanol, CH_3OH-A and CH_3OH-E, the kinetic temperature of the gas, and the H_2 density. For clump 3, we used a source size of 8″ as derived from

Table 2. Best-fit model results from the CH_3OH analysis towards the two clumps.

Source	S [″]	n_{H_2} [cm^{-3}]	T [K]	N_{CH_3OH} [cm^{-2}]	x_{CH_3OH}
clump 1	10	$6^{+4}_{-3} \times 10^6$	45^{+47}_{-17}	$3^{+1}_{-1} \times 10^{14}$	2×10^{-9}
clump 3	8	$5^{+5}_{-2} \times 10^6$	35^{+17}_{-15}	$3^{+3}_{-1} \times 10^{14}$	2×10^{-9}

The uncertainties correspond to the 3σ confidence level. The methanol column density (N) and fractional abundance relative to H_2 (x) is computed averaged over the extent of the clumps.

$H^{13}CN$ by Lis & Schilke (2003). For clump 1, the source size derived from the analysis of the $H^{13}CN$ emission is ~7″; however, other clumps fall partially in the ~20″ beam size of our observations (see Fig. 1). Therefore, we adopted a source size of 10″, which should take into account the emission of the other clumps at the edge of the beam. This corresponds to the assumption that all clumps in the Bar have similar physical properties.

The methanol spectra from the two clumps are very similar, although clump 3 is shifted in velocity by 0.7 km s^{-1} with respect to clump 1 ($v_{LSR} \sim 10.0$ km s^{-1} at clump 1, $v_{LSR} \sim 10.7$ km s^{-1} at clump 3). The spectra are characterised by narrow lines (~1.2 km s^{-1}), and no emission is detected in transitions with upper level energies greater than 85 K. As already discussed by Leurini et al. (2006), at the original velocity resolution of the APEX observations ($\Delta v \sim 0.12$ km s^{-1}), the CH_3OH ground state lines toward clump 1 have double-peaked profiles, probably because of the different clumps sampled by the beam. Since no double-peaked profile is detected in the IRAM data ($\Delta v \sim 0.38$ km s^{-1}) towards the same position, we smoothed the APEX spectra towards clump 1 to the same velocity resolution as the IRAM data. No double-peaked profile is detected towards clump 3. However, given the low signal-to-noise ratio of the APEX observations, we smoothed these data to a resolution of 0.5 km s^{-1}. The main difference in the methanol spectra of the two clumps is in the $1_1 \rightarrow 1_0$-A line at 303.4 GHz, which is much stronger in clump 3. Since this line has a lower level energy of 2.3 K, this suggests that clump 3 is colder than clump 1.

In Table 2, we report the results of the best-fit models for both clumps. For the column density, the total value of the column density for the two symmetry states is given. The high value for the spatial density suggests that the gas is close to thermal equilibrium, as verified by the results of our LVG calculations that show that most lines are partially subthermal. We carried out a χ^2 analysis to derive the uncertainties in the kinetic temperature, density, and column density. The values of the 3σ confidence levels of each parameters are reported in Table 2.

All lines are well fitted by the model, the only exception being the $5_1 \rightarrow 4_1$-E transition. The behaviour of this line remains unclear: in massive star-forming regions (Leurini et al. 2007) the $5_1 \rightarrow 4_1$-E is observed with an intensity roughly half of that of the blend of the $5_{\pm2} \rightarrow 4_{\pm2}$-$E$ lines, as expected since the three transitions have very similar energies. On the other hand, the $5_1 \rightarrow 4_1$-E transition in the Orion Bar has the same intensity of the $5_{\pm2} \rightarrow 4_{\pm2}$-$E$ lines blend, and cannot be fitted by our models.

For clump 3, the intensities of the ground state lines in the $6_k \rightarrow 5_k$ band, and in the $1_1 \rightarrow 1_0$-A line at 303.4 GHz are underestimated. The $1_1 \rightarrow 1_0$-A transition has a very low energy, and it is expected to be more intense in cold regions. This suggests that a two component model, with a layer of gas at a lower temperature, could be more appropriate for clump 3. However,

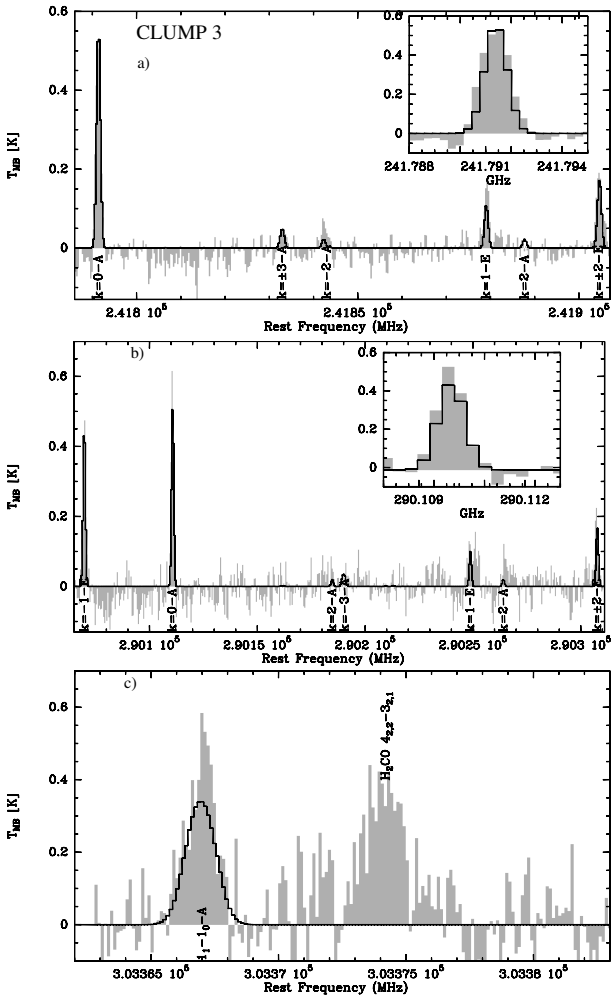

Fig. 2. Methanol spectra toward clump 3. **a)** 5→4 band observed with the IRAM 30 m telescope. **b)** 6→5 band observed with the APEX telescope. **c)** 1_1–1_0-A line (APEX). The synthetic spectra resulting from the fit are overlaid in black. The panel inserts show the $k = 0 - A$ lines in the two bands to illustrate how well the models fit the observed spectra.

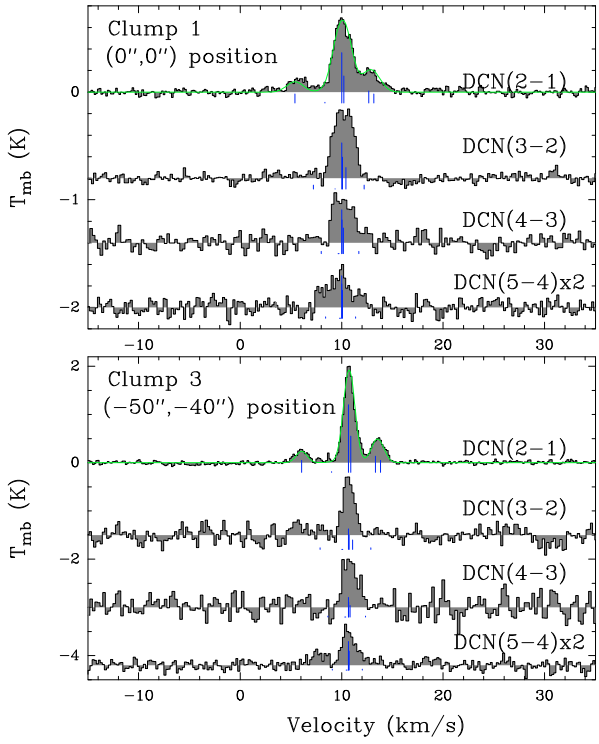

Fig. 3. DCN spectra observed towards the two groups of clumps. Hyperfine structure fits are displayed in green for the DCN(2–1) lines. A parasite line coming from the image sideband is visible in the DCN(5−4) data (clump 3). Because of the slight velocity difference between the two clumps, the parasite line is blended with the DCN(5−4) line on clump 1.

the reduced χ^2 for our model is 1.8, which is still reasonable for a simplified analysis.

The spectra for clump 1 and clump 3 are very similar. In Fig. 2, we therefore present the synthetic spectra for the best-fit model overplotted on the observed spectra for clump 3 only. The second feature in Fig. 2c is identified with ($4_{2,2}$ → $3_{2,1}$) H_2CO from the lower side band.

4. Deuterium fractionation in the clumps

Mapping of the DCN(4−3) emission across the Orion Bar with the APEX telescope shows that DCN emission originates in the $H^{13}CN$ clumps imaged by Lis & Schilke (2003). The overall distribution of DCN in the Bar will be the scope of a forthcoming paper (Parise et al. in prep.). Here, we study the chemistry at work in the clumps, and we therefore target selected transitions of deuterated molecules towards clump 1 and 3.

In the following subsections, we study the DCN excitation towards both clumps, present the detection of DCO^+ and HDCO towards clump 3, and estimate upper limits for the other molecules.

4.1. DCN and $H^{13}CN$ excitation

Figure 3 (respectively 4) shows the spectra of the several DCN (respectively $H^{13}CN$) transitions observed towards the clumps with the IRAM 30 m and the APEX telescopes. In the following subsections, we study the excitation of these two molecules, using LTE and LVG methods.

4.1.1. LTE analysis

Although the critical densities of the DCN and $H^{13}CN$ levels are quite high, several 10^5 to several 10^6 cm^{-3}, implying that the DCN and $H^{13}CN$ level populations may not be in LTE, it is instructive to draw rotational diagrams for the two groups of clumps. We corrected the observed line intensities for beam dilution effects by assuming a size of 7″ for clump 1, and 8″ for clump 3 (as derived by Lis & Schilke 2003). The rotational diagrams obtained are presented in Fig. 5, and the derived rotational temperatures and column densities are listed in Table 4.

Based on the assumption that the lines are optically thin, which is confirmed by the hyperfine structure analysis (see Sect. 4.1.2), the deviation from linearity in the rotational diagrams can be caused by either the very different beam sizes of the different observations, or to non-LTE effects. The first effect is not completely taken out by correcting for beam dilution, because the source may be more extended than the smallest beam. This could explain in particular why the DCN(3-2) transition (observed in the smallest beam) is weaker than the other transitions. Although the clumps are very dense (~5×10^6 cm^{-3}), the critical density of the different levels of the molecules is so high that the levels are not populated in LTE. $H^{13}CN$ seems to be even

Table 3. Observational results.

Position		clump 1 (0″, 0″)			clump 3 (−50″, −40″)	
Transition	$\int T_{\rm mb}dv$ (K km s^{-1})	*FWHM* (km s^{-1})	$V_{\rm lsr}$ (km s^{-1})	$\int T_{\rm mb}dv$ (K km s^{-1})	*FWHM* (km s^{-1})	$V_{\rm lsr}$ (km s^{-1})
DCN(2–1)	2.20 ± 0.04	1.9 (hfs)	10.0 ± 0.1	4.11 ± 0.05	1.3 (hfs)	10.7 ± 0.1
DCN(3–2)	1.62 ± 0.03	1.6 ± 0.1	10.0 ± 0.1	1.70 ± 0.11	1.1 ± 0.2	10.6 ± 0.1
DCN(4–3)	1.15 ± 0.07	1.3 ± 0.1	10.1 ± 0.1	1.75 ± 0.23	1.4 ± 0.3	10.8 ± 0.1
DCN(5–4)	0.25 ± 0.04*	1.9*	–	0.63 ± 0.10	1.7 ± 0.1	10.7 ± 0.1
$H^{13}CN$(1–0)	1.51 ± 0.05	1.8 (hfs)	10.1 ± 0.1	1.72 ± 0.05	1.6 (hfs)	10.6 ± 0.1
$H^{13}CN$(3–2)	4.49 ± 0.04	1.1 ± 0.1	10.0 ± 0.1	3.40 ± 0.04	1.3 ± 0.1	10.7 ± 0.1
$H^{13}CN$(4–3)	1.66 ± 0.06	1.8 ± 0.1	10.1 ± 0.1	1.72 ± 0.10	2.0 ± 0.1	10.9 ± 0.1
DCO^+(2–1)	<0.03 (3σ)	1.8⋆	–	0.12 ± 0.01	1.21 ± 0.14	10.7 ± 0.1
$H^{13}CO^+$(1–0)	0.40 ± 0.02	1.75 ± 0.12	10.1 ± 0.1	0.50 ± 0.02	2.20 ± 0.11	10.5 ± 0.1
HCO^+(1–0)	27.8**	2.08 ± 0.26	9.9 ± 0.3	35.3**	2.17 ± 0.03	10.5 ± 0.1
$HDCO(2_{11}–1_{10})$	–	–	–	0.041 ± 0.005	1.20 ± 0.16	10.4 ± 0.1
$H_2^{13}CO(2_{11}–1_{10})$	–	–	–	0.216 ± 0.014	1.91 ± 0.15	10.8 ± 0.1
C_2D(2–1)	–	–	–	<0.042 (3σ)	1.5⋆	–
CH_2DOH(2–1)	<0.008 (3σ)	1.8⋆	–	<0.011 (3σ)	1.5⋆	–
HDO	–	–	–	<0.093 (3σ)	1.5⋆	–
DNC(2–1)	–	–	–	<0.019 (3σ)	1.5⋆	–
HNC(4–3)	–	–	–	3.03 ± 0.06	2.1 ± 0.1	10.8 ± 0.1

* Line blended with a line coming from the image sideband. Flux was computed with a two-component Gaussian fit, keeping the line-width fixed.
** Integrated intensity computed without a Gaussian fit (the line is found to be non-Gaussian).
⋆ Assumed width to compute the upper limit on the flux.
Fluxes, *FWHM*, and $V_{\rm lsr}$ are computed by means of Gaussian fitting. Uncertainties given on integrated intensities are the errors in the Gaussian fit, and do not include the calibration uncertainties (assumed to be of the order of 15%).
All 3σ upper limits are computed using the following relation: $\int T_{\rm mb}dv < 3\times$ rms $\times \sqrt{FWHM \times \delta v}$.

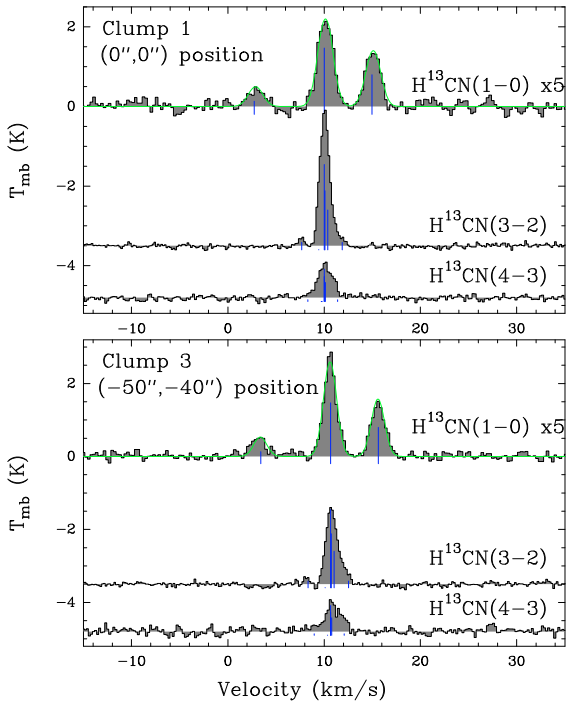

Fig. 4. $H^{13}CN$ spectra observed towards the two groups of clumps. Hyperfine structure fits are displayed in green for the $H^{13}CN$(1–0) lines.

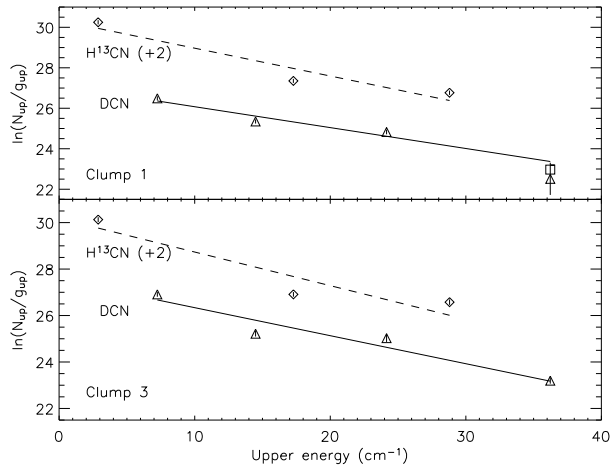

Fig. 5. Rotational diagrams for DCN (triangles) and $H^{13}CN$ (diamonds). The square represents the upper limit for the DCN(5–4) integrated intensity towards clump 1, computed as the total integrated intensity including the parasite line (see text).

further from LTE than DCN, which is consistent with the critical densities of $H^{13}CN$ being around a factor two higher than for DCN. The departure from LTE increases with the increasing upper level energy. The DCN(5–4) transition in clump 1 is in particular subthermally excited compared to the three lower energy transitions. This line is however blended with an unidentified line coming from the image sideband (at 350.554 GHz). The unidentified line is shifted away from the DCN(5–4) lines towards clump 3 due to the slight velocity difference between the two clumps.

The square in Fig. 5 represents the transition when all flux is assumed to come from DCN(5–4). This point is still too low in value compared to the three other transitions. It appears that

the blending of the line cannot account for the low intensity of the DCN(5−4) emission, and that the $J = 5$ level population is subthermal. After studying the hyperfine structure of the lower rotational transitions, we model the line emission using a non-LTE method.

4.1.2. Hyperfine structure

DCN and $H^{13}CN$ rotational transitions have an hyperfine structure, caused by the interaction of the electric quadrupole moment of the N nucleus ($I = 1$) with the molecular field gradient. This causes the transitions to be divided into several components, reducing the opacity at the line center. This effect is most important for the lower transitions, DCN(2–1) and $H^{13}CN$(1–0). From the relative intensity of the hyperfine components, it is possible to derive the opacity of the transition. This was done using the hfs method of the CLASS software[2]. This method fits the spectrum by assuming the same excitation temperature for each hyperfine component. The results of the fits are shown in Table 5.

The total opacity of the DCN(2–1) is found to be low. When the opacity is tightly enough constrained so that the T_{ex} can be accurately derived, the excitation temperature is rather low (Table 5). It should however be noted that the derived T_{ex} value is a lower limit because of beam dilution. The excitation temperature provides a lower limit to the kinetic temperature, as the level populations might not be thermalized, because of the high critical densities of each transition. The same holds for $H^{13}CN$(1–0). The transition is optically thin at both positions, and the excitation temperatures are also rather low.

4.1.3. DCN and $H^{13}CN$ column densities

To derive column densities, we used a standard LVG code. The hyperfine structure of the lower levels is not explicitly taken into account. However, to account for the reduced opacity caused by the hyperfine splitting, we replaced the escape probability by a weighted mean of the escape probabilities of the hyperfine components: $\beta = \sum_i f_i \frac{1 - e^{-f_i \tau_{tot}}}{f_i \tau_{tot}}$. For both isotopologues, we used collision coefficients calculated for HCN-He by Wernli & Faure (2009, in prep.). These collision coefficients were uniformly scaled by a factor 1.37 (square root of the ratio of the reduced mass of the HCN-He to HCN-H_2 systems) to approximate HCN-H_2 collisions. This approximation is generally supposed by astronomers to be valid for HCN-pH_2 collisions, as para-H_2 has a spherical symmetry in its $J = 0$ state. Theoretical computations have shown that the accuracy of this assumption is however limited, the discrepancy for individual rates reaching up to a factor of two for particular systems (H_2O–H_2/He, Phillips et al. 1996; CO–H_2/He, Wernli et al. 2006; HC_3N–H_2/He, Wernli et al. 2007; SiS–H_2/He, Lique et al. 2008), or even higher (NH_3–H_2/He, Maret et al. 2009). This is however the only solution as long as HCN–H_2 collision rates are not available.

Input parameters for an LVG code are n_{H_2}, T, and $N_{mol}/\Delta v$. Comparing modelled line temperatures with observations brings another parameter into play, the beam filling factor. On the observational side, we wish to fit simultaneously for each molecule the observations of all available transitions and the opacity derived by the hfs method for the lower transition. There are thus 5 observables for DCN and 4 for $H^{13}CN$. It is statistically rather meaningless to try to fit a sample of four/five observations with a 4-parameter model. We therefore use independently determined information for the source size (Lis & Schilke 2003), and the H_2 density as derived from methanol observations (see Sect. 3.2), and only fit the temperature and the DCN and $H^{13}CN$ column densities.

[2] GILDAS package, http://www.iram.fr/IRAMFR/GILDAS/

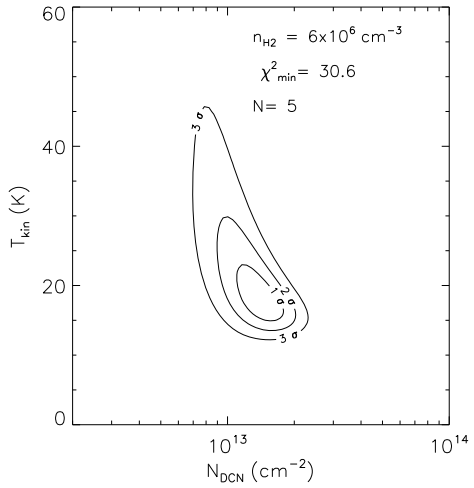

Fig. 6. LVG analysis results for the DCN molecule towards Clump 1.

Table 4. Results of rotational diagrams and LVG analysis.

Rotational diagram					
Source	T_{rot}(DCN) (K)	N_{DCN} (10^{13} cm^{-2})	T_{rot}($H^{13}CN$) (K)	$N_{H^{13}CN}$ (10^{13} cm^{-2})	DCN/HCN* (%)
clump 1	14.0 ± 1.1	1.4 ± 0.3	10.5 ± 0.4	3.1 ± 0.4	0.7 ± 0.2
clump 3	11.9 ± 0.5	1.9 ± 0.3	9.9 ± 0.4	2.5 ± 0.3	1.1 ± 0.2
LVG analysis					
Source	T_{kin} [DCN] (K)	N_{DCN} (10^{13} cm^{-2})	T_{kin}[$H^{13}CN$] (K)	$N_{H^{13}CN}$ (10^{13} cm^{-2})	DCN/HCN* (%)
clump 1	18^{+5}_{-3}	$1.4^{+0.4}_{-0.3}$	21^{+3}_{-2}	$8.2^{+2.8}_{-2.2}$	0.3 ± 0.1
clump 3	32^{+13}_{-7}	$1.0^{+0.4}_{-0.3}$	26^{+4}_{-3}	$1.9^{+0.4}_{-0.3}$	0.8 ± 0.3

Given error bars are 1σ. We note that the T_{kin} derived from LVG analysis of DCN and $H^{13}CN$ are consistent within the 3σ uncertainty range with the T_{kin} values derived from methanol.
* Assuming HCN/$H^{13}CN$ = 70 (Wilson 1999).

Figure 6 shows, as an example, the χ^2 analysis for fitting LVG models for the DCN molecule towards clump 1. The χ^2 was computed by using the 4 DCN transitions, weighted by uncertainties including a 15% calibration uncertainty in the integrated flux, as well as the opacity of the DCN(2−1) line as derived in Sect. 4.1.2. The derived kinetic temperature is consistent within its 3σ uncertainty range with the one derived from the methanol analysis. The DCN column density also compares very well with the rotational diagram result. The 1σ confidence interval for the two parameters is shown in Table 4. We analyzed in the same way the DCN emission towards clump 3 as well as the $H^{13}CN$ towards both clumps. The results are all shown in Table 4.

4.2. Low DCO^+ emission

DCO^+(2–1), $H^{13}CO^+$(1–0), and HCO^+(1–0) were observed towards the two clumps. The spectra are presented in Fig. 7. By comparison with $H^{13}CO^+$(1–0), HCO^+(1–0) is found to be optically thin. The observed parameters are listed in Table 3. Note

Table 5. Results of the hyperfine structure fit.

Source	Line	v_{lsr} (km s^{-1})	*FWHM* (km s^{-1})	$T_{mb} \times \tau_{tot}$ (K)	τ_{tot}	T_{ex} (K)	n_{cr} (50 K) (cm^{-3})
Clump 1	DCN(2–1)	10.01 ± 0.02	1.90 ± 0.04	1.2 ± 0.1	0.7 ± 0.2	5.0 ± 1.8	9.1×10^5
	H^{13}CN(1–0)	10.13 ± 0.02	1.78 ± 0.07	0.92 ± 0.09	0.56 ± 0.41	4.6 ± 3.8	1.8×10^5
Clump 3	DCN(2–1)	10.66 ± 0.01	1.30 ± 0.02	2.8 ± 0.1	0.1 ± 0.4	31.5 ± 127	9.1×10^5
	H^{13}CN(1–0)	10.62 ± 0.02	1.61 ± 0.03	0.96 ± 0.02	0.10 ± 0.04	12.7 ± 5.3	1.8×10^5

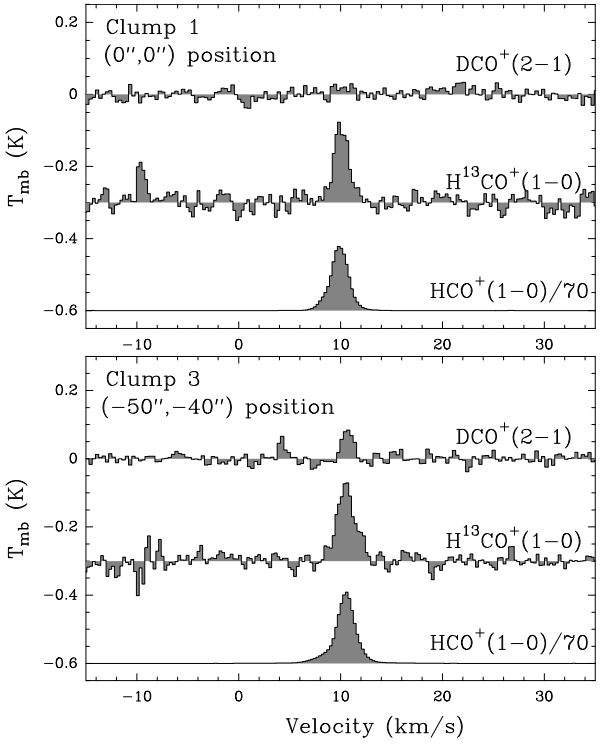

Fig. 7. DCO$^+$, H^{13}CO$^+$, and HCO$^+$ spectra.

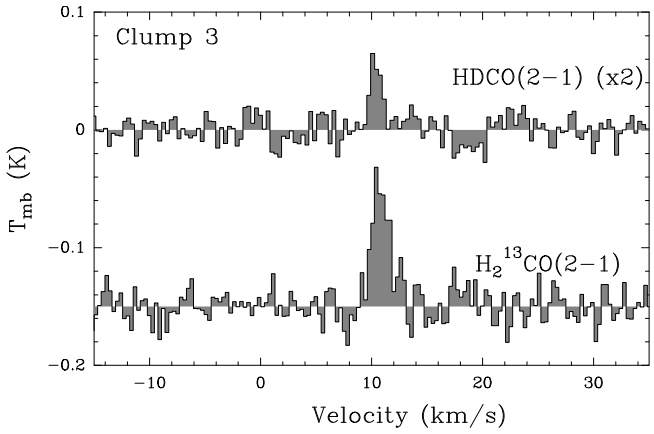

Fig. 8. HDCO and $H_2^{13}CO$ detected towards clump 3.

that toward clump 3 the linewidth of the H^{13}CO$^+$ and HCO$^+$ lines are significantly larger than the HCN and DCN linewidths (as determined from the hyperfine structure fit). The thermal broadening expected for H^{13}CO$^+$ at 50 K is 0.27 km s^{-1}, and 0.47 km s^{-1} at 150 K, the temperature characteristic of the interclump gas. This implies that HCO$^+$ and H^{13}CO$^+$ are also present in the warmer interclump gas, in agreement with the interferometric studies of Young Owl et al. (2000) and Lis & Schilke (2003), who claimed that a large fraction of the emission of H^{13}CO$^+$(1–0) is extended and thus filtered out by the interferometer.

On the other hand, we do not expect deuterated molecules to be present at all in the hot interclump gas in steady-state. The fact that the main isotopomers are likely to trace both the two gas components implies that the D/H ratio derived from the observations should be considered as a lower limit.

We estimate column densities towards the clumps (assuming sizes of 7″ and 8″ for clump 1 and 3 respectively) for different rotational temperatures, assuming that all emission comes from the clumps. Although DCO$^+$ and H^{13}CO$^+$ column densities vary by a factor between two and three for temperatures between 20 and 70 K, the abundance ratio is less affected by the temperature uncertainty (by less than a factor of 1.5, see Table 6)

Can we quantify how much of the HCO$^+$ emission originates in the clumps? Hogerheijde et al. (1995) modelled multi-frequency transitions of several molecules with a two-phase (interclump + clump) model, and they concluded that 10% of the column density of the material is in the clumps. We can then estimate the clump contribution to H^{13}CO$^+$ emission. Since the emission is probably dominated by the interclump gas, we estimate the column density of HCO$^+$ by assuming a temperature of 150 K. For clump 3, we then find a column density of H^{13}CO$^+$ of 6.2×10^{13} cm^{-2}. If the clump represents 10% of the column density, then N(H^{13}CO$^+$) $\sim 6 \times 10^{12}$ cm^{-2} in the clump, which is roughly a factor of two to three lower than we estimated. We may thus underestimate the DCO$^+$/HCO$^+$ by a factor of up to three.

4.3. Detection of HDCO

To test the possibility that the deuteration in the clumps originates in chemical processes involving CH_2D^+, we targeted HDCO, a molecule synthesized in the gas phase via the CH_2D^+ route, by the following reactions (Turner 2001; Roueff et al. 2007):

$$CH_2D^+ + H_2 \rightarrow CH_4D^+ \quad (4)$$

$$CH_4D^+ + e^- \rightarrow CH_2D + H_2 \quad (5)$$

$$CH_2D + O \rightarrow HDCO + H. \quad (6)$$

We detected the HDCO(2–1) transition towards clump 3 (Fig. 8). The line has a v_{lsr} of 10.4 km s^{-1}, consistent with other lines detected towards this clump. The line width (1.2 km s^{-1}) is also similar to those of other deuterated species (DCN, DCO$^+$), making the detection of HDCO rather secure. We also detected the $H_2{}^{13}CO$(2–1) line towards the same position.

We computed the column density of the two molecules using the LTE approximation. The column densities vary by a factor of three depending on the assumed temperature of between 20 and 70 K. However, as the two observed lines have similar energies, the HDCO/$H_2{}^{13}CO$ ratio is less sensitive to the

Table 6. Rotational analysis for HCO^+ and isotopologues. Upper limits are 3σ.

	clump 1			clump 3		
T_{rot}	N_{DCO^+} (cm^{-2})	$N_{H^{13}CO^+}$ (cm^{-2})	N_{DCO^+}/N_{HCO^+} [1]	N_{DCO^+} (cm^{-2})	$N_{H^{13}CO^+}$ (cm^{-2})	N_{DCO^+}/N_{HCO^+} [1]
20 K	$<1.6\times10^{11}$	1.0×10^{13}	$<2.3\times10^{-4}$	$(5.0\pm0.8)\times10^{11}$	$(9.9\pm0.1)\times10^{12}$	$(7.3\pm1.4)\times10^{-4}$
30 K	$<2.0\times10^{11}$	1.4×10^{13}	$<2.0\times10^{-4}$	$(6.2\pm1.0)\times10^{11}$	$(1.4\pm0.2)\times10^{13}$	$(6.4\pm1.3)\times10^{-4}$
40 K	$<2.4\times10^{11}$	1.8×10^{13}	$<1.9\times10^{-4}$	$(7.5\pm1.2)\times10^{11}$	$(1.8\pm0.2)\times10^{13}$	$(6.0\pm1.1)\times10^{-4}$
50 K	$<2.8\times10^{11}$	2.2×10^{13}	$<1.8\times10^{-4}$	$(8.9\pm1.4)\times10^{11}$	$(2.2\pm0.2)\times10^{13}$	$(5.9\pm1.0)\times10^{-4}$
70 K	$<3.7\times10^{11}$	3.1×10^{13}	$<1.7\times10^{-4}$	$(1.2\pm0.2)\times10^{12}$	$(3.0\pm0.3)\times10^{13}$	$(5.7\pm1.1)\times10^{-4}$

[1] We assume $HCO^+/H^{13}CO^+ = 70$ (Wilson 1999).

temperature, varying only by a factor of 1.2 over the whole temperature range, which lies within the error bar of the determined ratio. In Table 7, we give the column densities and D/H ratio for a fixed temperature of 35 K (as inferred by the analysis of the CH_3OH emission). We assume again that $H_2{}^{13}CO/H_2CO = 70$ (Wilson 1999).

One should note that H_2CO is also partly tracing the inter-clump gas (Leurini et al. 2006; Leurini et al. submitted). The derived $HDCO/H_2CO$ ratio above is thus to be considered to be a lower limit (see discussion in Sect. 5.3).

4.4. Upper limits to other interesting deuterated molecules

In the following, we derive upper limits to the fractional abundances of other deuterated molecules that were not detected. The discussion of the results is left to Sect. 5.

4.4.1. C_2D

C_2D is another molecule believed to form in the gas phase from CH_2D^+. Roueff et al. (2007) predicted an D/H ratio for this molecule of 3.9×10^{-2}, and an abundance of 6.6×10^{-11} with respect to H_2, in their low metal model at 50 K.

The $J = 2-1$ band was observed towards clump 3. The VESPA correlator at the IRAM telescope showed unfortunately a lot of platforming. Using the 1 MHz filter bank, the lines are not detected, and the rms is 8 mK (T_{mb} scale) at a resolution of 2.1 km s^{-1}. Assuming a linewidth of 1.5 km s^{-1} (as found in HCN and DCN observations), we derive the flux upper limit listed in Table 3. Assuming a T_{rot} of 35 K, this corresponds to an upper limit to the C_2D column density of 2.5×10^{13} cm^{-2}, and an upper limit to the fractional abundance of 2×10^{-10}, compatible with the prediction of Roueff et al. (2007).

4.4.2. DNC

DNC is synthesized in the gas phase, mainly from a route involving the H_2D^+ ion, as opposed to DCN, which can be synthesized from CH_2D^+ (Turner 2001; Roueff et al. 2007). We searched for the 2–1 transition of this species, to constrain the importance of the H_2D^+ chemistry in clump 3. We did not detect the line, at a rms noise level of 9 mK (T_{mb} scale) and a resolution of 0.31 km s^{-1}. We derive the flux upper limit listed in Table 3. This corresponds to an upper limit of 1.5×10^{11} cm^{-3} for the DNC column density (assuming $T_{rot} = 35$ K), and an upper limit to the abundance relative to H_2 of 1.0×10^{-12}. Assuming that the HNC(4–3) line is optically thin, we find that $N_{HNC} = 1.05\times10^{13}$ cm^{-2}. This must be considered as a lower limit if HNC(4–3) is not optically thin. This translates into an upper limit of $DNC/HNC < 1.4\times10^{-2}$ (3σ). This upper limit does not provide as tight a constraint as the deuteration ratios measured in HCN, because HNC is found to be more than three orders of magnitude less abundant than HCN. The very high HCN/HNC ratio in the clump is to our knowledge one of the highest observed so far.

4.4.3. CH_2DOH

We searched for monodeuterated methanol, which is believed to trace the evaporation of highly deuterated ices (Parise et al. 2002, 2004, 2006). We looked for the 2_K-1_K rotational band at 89 GHz, corresponding to low energy transitions. CH_2DOH was not detected towards any of the two clumps. Rms levels of 4 mK toward clump 1 and 6 mK toward clump 3 (T_{mb} scale) were reached, at a 0.26 km s^{-1} resolution. Assuming a linewidth of 1.8 (resp. 1.5) km s^{-1} for clump 1 (resp. 3), we derive the upper limit to the integrated intensity listed in Table 3. This corresponds to an upper limit of 1.9×10^{14} cm^{-2} to the CH_2DOH column density in clump 3, i.e., an upper limit to the fractional abundance of 1.5×10^{-9}.

4.4.4. HDO

The HDO line at 241 GHz was searched for towards clump 3 but not detected, at a noise level of 47 mK (rms, T_{mb} scale), and a resolution of 0.3 km s^{-1}. The associated upper limit for the integrated line intensity given in Table 3 corresponds to an upper limit of 4.4×10^{13} cm^{-2} for the HDO column density, i.e., an upper limit to the abundance of 3.4×10^{-10}.

5. Discussion

The main results of this study are the confirmation by multi-transition observations of the significant deuterium fractionation of HCN found by Leurini et al. (2006), as well as the detection of significant fractionation of HDCO in dense clumps in the Orion Bar PDR that are too warm for deuteration to be sustained by the H_2D^+ precursor. In the following, we consider the possible explanations of this high deuteration: products evaporated from ices surrounding dust grains, or gas-phase products. This study can also help us to understand the chemistry at work in PDRs.

5.1. Grain evaporation?

One plausible origin for highly deuterated molecules is the evaporation of ices surrounding dust grains. Highly deuterated methanol, formaldehyde and water are observed in hot cores (e.g., Jacq et al. 1988; Comito et al. 2003) and hot corinos

Table 7. Summary of column densities, abundances, and D/H ratios in the observed molecules.

Molecule	clump 1 N (cm^{-2})	clump 1 x (cm^{-3})	clump 1 XD/XH	clump 3 N (cm^{-2})	clump 3 x (cm^{-3})	clump 3 XD/XH
$H^{13}CN$	$(3.1 \pm 0.4) \times 10^{13}$	1.9×10^{-10}		$(2.5 \pm 0.3) \times 10^{13}$	1.9×10^{-10}	
DCN	$(1.4 \pm 0.3) \times 10^{13}$	8.8×10^{-11}	0.7 ± 0.2 %	$(1.9 \pm 0.3) \times 10^{13}$	1.5×10^{-10}	1.1 ± 0.2 %
$H^{13}CO^+$	$(2.0 \pm 1.0) \times 10^{13}$	1.3×10^{-10}		$(1.6 \pm 0.2) \times 10^{13}$	1.2×10^{-10}	
DCO^+	$<2.2 \times 10^{11}$	$<1.4 \times 10^{-12}$	$< 2 \times 10^{-4}$	$(6.9 \pm 1.1) \times 10^{11}$	5.3×10^{-12}	$(6.1 \pm 1.1)\ 10^{-4}$
$H_2{}^{13}CO$	–	–	–	$(1.2 \pm 0.1) \times 10^{13}$	9.2×10^{-11}	
HDCO	–	–	–	$(4.8 \pm 0.8) \times 10^{12}$	3.7×10^{-11}	0.6 ± 0.1%
C_2D	–	–	–	$<2.5 \times 10^{13}$	$<2 \times 10^{-10}$	–
HNC	–	–	–	1.1×10^{13}		
DNC	–	–	–	$<1.5 \times 10^{11}$	$<1 \times 10^{-12}$	<1.4 %
CH_2DOH	$<1.7 \times 10^{14}$	$<1.1 \times 10^{-9}$	–	$<1.9 \times 10^{14}$	$<1.5 \times 10^{-9}$	–
HDO	–	–	–	$<4.4 \times 10^{13}$	$<3.4 \times 10^{-10}$	–

We assumed that T_{rot} = 35 K for species detected with only one transition.

(Parise et al. 2002, 2004, 2005, 2006), and are assumed to be remnants of the cold prestellar phase.

In particular, methanol is believed to form primarily on dust grains, since the gas-phase production routes for this molecule are inefficient. The same may also be true for water, the main constituent of ices surrounding dust grains. Deuterated isotopologues of these molecules may thus trace surface chemistry processes that enhance the deuterium content of these species, because the accreting atomic D/H ratio is much higher than the elemental D/H ($\sim 10^{-5}$). Atomic accretion onto dust grains and surface reactions take place in cold environments, i.e., in conditions that also favor a high atomic D/H. Although the characteristics of the thermal history experienced by the gas in the Orion Bar in the past remain unclear (are the clumps remnants of high density clumps of the cold molecular cloud, which are still shielded from the PDR radiation?), it may be possible that we are witnessing inside the clumps the evaporation of ices that formed during the cold molecular cloud phase. In this case, we would expect the composition of the ices to be comparable to the ones evaporated in hot corinos, i.e., with high CH_2DOH/CH_3OH ratios.

The temperature of the grains should follow closely the gas temperature (typically <50 K) in the clumps, because of the high density in the clumps (Kruegel & Walmsley 1984). Although this temperature is high enough to sublimate CO ices ($T_{evap} \sim 20$ K), it is not high enough to sublimate polar ices dominated by H_2O ($T_{evap} \sim 100$ K). Pure HCN ices are expected to sublimate in the ISM conditions at temperatures ~65 K (extrapolation from the sublimation temperatures in comets from Prialnik 2006). However, HCN is only a minor constituent of ices in the objects in which it was detected (<3% of water in W33A, 0.25% of water in Hale Bopp, Ehrenfreund & Charnley 2000). It will thus behave as a small impurity of the water ice, and its sublimation will be dominated by the sublimation of H_2O. It is thus rather unlikely that evaporation plays an important role in the warm clumps, except maybe on the clump surfaces.

The low relative abundance of methanol (2×10^{-9}) compared to its abundance in hot corinos ($\sim 10^{-7}$, Maret et al. 2005) may be a further sign that *thermal* evaporation is not the dominant chemical process, but rather that gas-phase chemistry is the most significant mechanism responsible for the enhanced deuteration levels. We note that grain chemistry models including non-thermal desorption of methanol are enough to explain these relatively low abundances of methanol (Garrod et al. 2007). Of course it is also possible that evaporated ices become photodissociated in the PDR, and this effect will be studied in more detail in a forthcoming paper (Parise et al. in prep). We focus here on an alternative explanation, assuming that gas phase reactions are more predominant.

5.2. Gas-phase chemistry?

The low temperature of the clumps with respect to the sublimation temperature of water ices infers that thermal ice evaporation does not play a predominant role in the clumps. At the same time, the grain temperature (which, at these high densities, should follow the observed gas temperature) is too high for CO to stick efficiently onto dust grains, preventing efficient grain chemistry taking place. The present chemistry is thus likely dominated by gas-phase processes, and the clumps may be in this sense remnants of the molecular cloud, which have been warmed up to temperatures higher than for typical molecular clouds, because of their location behind the photoionising front. The CH_3OH abundance, in particular, is similar to that measured towards the TMC-1 dark cloud (3×10^{-9}, Smith et al. 2004), and this molecule appears to be a remnant of grain chemistry happening during the colder era of the cloud, followed by non-thermal desorbing processes (Garrod et al. 2007). This possibility may be tested further by observing the D/H ratio in methanol. A formation of methanol during the cold molecular cloud phase is expected to lead to high CH_2DOH/CH_3OH ratios, as measured e.g., in prestellar cores (between 5% and 30% Bacmann et al. 2007). Unfortunately, the upper limit that we derive here ($CH_2DOH/CH_3OH < 0.8$) does not provide a sufficiently tight constraint, and further insight will require significantly deeper integrations, for which the sensitivity of ALMA will be needed.

For other molecules that can also form in the gas-phase, gas-phase processes are likely to be predominant. To test the hypothesis that gas-phase chemistry is the dominant process in the clumps, in the remaining discussion we compare the observed abundances and D/H ratios to the results of a pure steady-state gas-phase model. In particular, we are interested in whether a high DCN/HCN ratio, low DCO^+/HCO^+ ratio and the detection

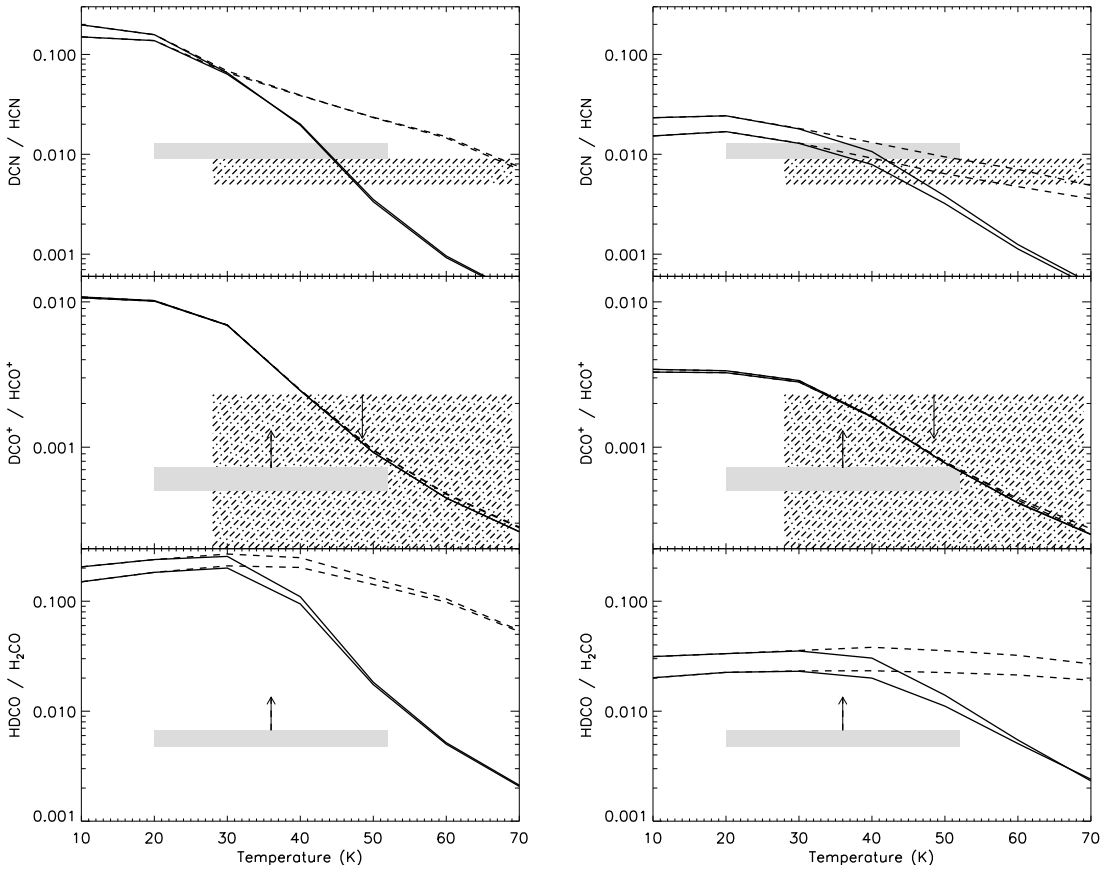

Fig. 9. Predictions of the D/H ratio for several molecules, as a function of the temperature, and observed ratios for clump 1 (dash-dot filling) and for clump 3 (grey filling). Model predictions from *saa* model (solid curves) and *theo* model (dashed curves) are computed for densities 3×10^6 and 1×10^7 cm^{-3}. *Left panel*: low-metal elemental abundances. *Right panel*: warm core elemental abundances (see text and Roueff et al. 2007).

of HDCO can be explained in the framework of a simple steady-state model.

5.3. Comparison to gas-phase model

In the following, we compare the observed fractionation and relative abundances of molecules to the predictions of a pure gas-phase model, based on an updated version of the chemical model described by Roueff et al. (2007). The new model takes into account the new branching ratios of the N_2H^+ dissociative recombination (Molek et al. 2007), and computes the pre-exponential factors of the reverse reactions involved in the deuterium fractionation of CH_3^+ with the proper factors involved in the translational partition functions. In addition, we have included the branching ratios of the electronic recombination of HCO^+ from Amano (1990), where the channel towards CO is found to be predominant. The radiative association reactions of CH_3^+ and deuterated substitutes with H_2 have been derived from the theoretical predictions of Bacchus-Montabonel et al. (2000), who provide values for different temperatures.

The exothermicity of the $CH_3^+ + HD$ reaction and subsequent deuteration steps are not well constrained. These exothermicities were derived experimentally by Smith et al. (1982). However, theoretical assessments from zero-point energies lead to higher barriers. This has the effect of allowing deuteration to remain efficient at even higher temperatures (up to 70 K). In the following, we compare our observations to two models, calculated by using the experimental values from Smith et al. (1982, *saa* model) and the exothermicities computed theoretically from zero-point energies (*theo* model). The respective exothermicities assumed in the models are listed in Table 8.

Table 8. Exothermicities used in the two different chemical models.

Reaction	Exothermicity saa model	Exothermicity theo model
$CH_3^+ + HD \Leftrightarrow CH_2D^+ + H_2$	370 K	670 K
$CH_2D^+ + HD \Leftrightarrow CHD_2^+ + H_2$	369 K	433 K
$CHD_2^+ + HD \Leftrightarrow CD_3^+ + H_2$	379 K	443 K
$CH_3^+ + D_2 \Leftrightarrow CHD_2^+ + H_2$	713 K	1005 K
$CH_3^+ + D_2 \Leftrightarrow CH_2D^+ + HD$	319 K	592 K
$CH_2D^+ + D_2 \Leftrightarrow CD_3^+ + H_2$	599 K	564 K
$CH_2D^+ + D_2 \Leftrightarrow CHD_2^+ + HD$	317 K	354 K
$CHD_2^+ + D_2 \Leftrightarrow CD_3^+ + HD$	290 K	151 K

Figure 9 shows the observed ratios towards clump 1 and 3 respectively, as well as the predicted ratios of the chemical models. The solid curves correspond to the *saa* model, and the dashed curves to the *theo* model. The two curves for each model correspond to the densities 3×10^6 and 10^7 cm^{-3} (in order of increasing D/H ratio). The grey filling delimitates the observed values (1σ) or their upper limits (3σ), and the temperature range (3σ) derived from the CH_3OH analysis. We computed the model predictions for the two different sets of elemental abundances used in Roueff et al. (2007). The "warm core" elemental abundances are representative of a mostly undepleted gas, while the "low metal" case, shown to lead to the closest agreement to observations towards dense molecular clouds (Graedel et al. 1982),

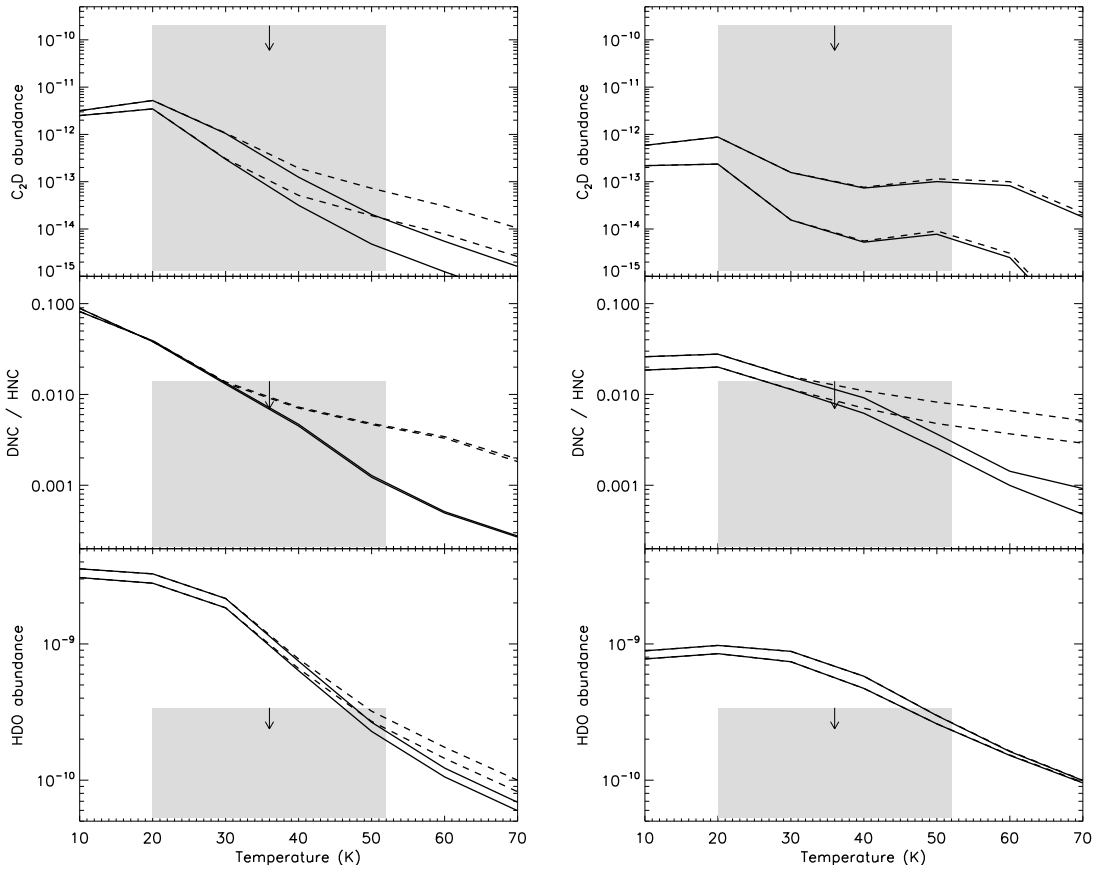

Fig. 10. Undetected molecules towards clump 3. Same plotting codes as for Fig. 9.

involves moderate depletions of C, N, and O, and strong depletions of S and Fe.

The models all show a decreasing fractionation with increasing temperature. In the case of clump 1 (Fig. 9), DCO^+ was not detected, and thus we have only an upper limit to the observed DCO^+/HCO^+ ratio. The observed DCN/HCN ratio is consistent with the model prediction for a clump temperature of ∼45 K, for the *saa* model with low-metallicity elemental abundances. The *theo* model tends to overestimate the DCN/HCN ratio, requiring temperatures >70 K to reproduce the observed ratio, which are still consistent but at the high end of the uncertainty range of the temperature determined from the methanol observations. Both models with warm core elemental abundances also qualitatively reproduce the DCN/HCN for a reasonable temperature range. The upper limit to the DCO^+/HCO^+ ratio is for this clump a very tight constraint. Depending on the model, it infers that $T > 33$ K or $T > 40$ K, which is consistent with the temperatures given by the DCN/HCN ratios.

In the case of clump 3 (Fig. 9), both DCO^+/HCO^+ and $HDCO/H_2CO$ ratios were measured. The derived fractionation ratios were estimated by assuming that the main isotopologue only traces the clump. However, there is some evidence that H_2CO and HCO^+ are also present in the interclump medium. The case for HCO^+ was discussed in Sect. 4.2, where we argued that we may have underestimated the DCO^+/HCO^+ ratio by up to a factor of three. H_2CO has been shown to be roughly as abundant in the clumps as in the interclump gas by Leurini et al. (submitted), who derive an H_2CO column density of between 6×10^{13} and 6×10^{14} cm^{-3} in the interclump gas, and of $(2.8–5.4) \times 10^{14}$ cm^{-3} towards clump 1, which is up to a factor of three lower than our estimate from $H_2^{13}CO$ towards clump 3. We may thus be overestimating the H_2CO abundance in clump 3 by a factor of two to three.

As a consequence, the ratios that we have derived should only be considered as lower limits to the true ratios in the clumps (represented by the ascending arrows in Fig. 9). We note that this is not the case for the DCN/HCN ratio, because $H^{13}CN$ has been shown to trace only the clumps (Lis & Schilke 2003). In the case of clump 3, the DCN/HCN ratio infers a temperature of ∼45 K (low-metal elemental abundances), or 20-50 K (warm core conditions). Both DCO^+/HCO^+ and $HDCO/H_2CO$ lower limits are in principle consistent with the model. However, in the case of the low-metal *saa* model, for a temperature of 45 K, agreement with the model would require that we increase the H_2CO abundance in the clump by a factor of six, which does not seem consistent with the study of Leurini et al. (submitted). For this clump, closer qualitative agreement is found with the models with warm core elemental conditions. It is also instructive to see if the upper limits for other deuterated molecules (C_2D, DNC, HDO) are consistent with the models (Fig. 10). In the case of HDO and C_2D, where we have no observations of the main isotopologue, we compare the abundances directly with the model predictions. The C_2D upper limits do not provide tight constraints – a two orders of magnitude increase in the sensitivity would be required to provide significant constraints. The DNC/HNC upper limits point to $T > 30$ K. But the molecule for which the tightest constraint can be obtained is certainly HDO, whose non-detection is consistent with the models only for $T > 40–50$ K. That the HDO abundance seems to be consistent and even rather on the lower side of the model predictions is certainly a good hint that *thermal* evaporation is not playing a dominant role in injecting water molecules into the gas-phase.

As a conclusion from this comparison, we find good qualitative agreement between the observations and pure steady-state gas-phase models. Although this comparison is obviously limited, because the physical structure (temperature and density gradient) of the clump is not taken into account, and because the chemistry is only computed at steady-state, it shows that the scenario of warm gas phase deuterium chemistry is viable for explaining the high deuteration ratios observed in DCN towards the Orion Bar clumps.

The comparison with the models is unfortunately limited by our poor handle on the clump temperature. Good probes of the temperature are usually the inversion lines of the NH_3 molecule. NH_3 was mapped in the Orion Bar by Batrla & Wilson (2003) with a single-dish telescope. Although they find that the NH_3 emission comes mostly from the same regions as the HCN emission, they find high kinetic temperatures ($T > 100$ K) and argue that ammonia is located in the surface layers of the clumps, where icy mantle around dust grains evaporate. The traced temperature is thus rather typical of that of the interclump gas, and NH_3 is therefore not a good probe of the clump temperature. Deeper observations of several lines of CH_3OH, including high-J transitions might allow us to constrain the temperature more tightly.

On the model side, a more detailed treatment taking into account photodissociation in the PDR is the next step to take.

6. Conclusions

We have presented observations of deuterated molecules towards two dense clumps in the Orion Bar photodissociation region. These observations were designed to confirm and understand the origin of the DCN emission first detected in this region by Leurini et al. (2006). We confirmed by the observation of four transitions of DCN the detection of this molecule towards one clump, and detected it towards a second clump of the Orion Bar. We also detected DCO^+ and HDCO towards this second clump, and provided upper limits to the abundance of other relevant deuterated molecules. From the observation of these several species, formed by chemistry induced either by H_2D^+ or CH_2D^+, we find evidence based on a pure gas-phase chemistry model that the main ion responsible for deuteron transfer in the Orion Bar is CH_2D^+, as opposed to previously observed cases of colder regions or hot cores where H_2D^+ was the main actor (in the case of hot cores, deuterium fractionation is believed to be a fossil of cold chemistry in the earlier cold evolutionary phase, preserved into ice mantles). The luke-warm conditions in the Orion Bar clumps thus allowed us to observationally test chemical models in a different temperature range than most previous studies dealing with deuterium fractionation. A more refined understanding of the chemistry at work in the Orion Bar will require more detailed chemical modelling, coupling PDR models with gas-grain chemical networks.

Acknowledgements. We are very grateful to the APEX staff, in particular P. Bergman and A. Lundgren, for performing part of the APEX observations presented here. B.P. thanks M. Wernli for providing the HCN-He collision rates before publication, and for enlightening discussions. B.P. acknowledges fruitful discussions with A.G.G.M. Tielens and R. Garrod, and enlightening comments on statistics from Edward Polehampton and Didier Pelat. This work was funded by a Alexander von Humboldt research fellowship and by the German *Deutsche Forschungsgemeinschaft, DFG* Emmy Noether project number PA1692/1-1. D.C. Lis is supported by the U.S. National Science Foundation, award AST-0540882 to the Caltech Submillimeter Observatory.

References

Amano, T. 1990, J. Ch. Ph., 92, 6492
Asvany, O., Schlemmer, S., & Gerlich, D. 2004, ApJ, 617, 685
Bacchus-Montabonel, M., Talbi, D., & Persico, M. 2000, J. Phys. B, 33, 955
Bacmann, A., Lefloch, B., Parise, B., Ceccarelli, C., & Steinacker, J. 2007, in Molecules in Space and Laboratory
Batrla, W., & Wilson, T. L. 2003, A&A, 408, 231
Caselli, P., van der Tak, F. F. S., Ceccarelli, C., & Bacmann, A. 2003, A&A, 403, L37
Caselli, P., Vastel, C., Ceccarelli, C., et al. 2008, A&A, 492, 703
Comito, C., Schilke, P., Gérin, M., et al. 2003, A&A, 402, 635
Ehrenfreund, P., & Charnley, S. B. 2000, ARA&A, 38, 427
Flower, D. R., Pineau des Forêts, G., & Walmsley, C. M. 2004, A&A, 427, 887
Garrod, R. T., Wakelam, V., & Herbst, E. 2007, A&A, 467, 1103
Gerlich, D., Herbst, E., & Roueff, E. 2002, Planet. Space Sci., 50, 1275
Graedel, T. E., Langer, W. D., & Frerking, M. A. 1982, ApJS, 48, 321
Güsten, R., Nyman, L. Å., Schilke, P., et al. 2006, A&A, 454, L13
Hatchell, J., Millar, T. J., & Rodgers, S. D. 1998, A&A, 332, 695
Herbst, E., Adams, N. G., Smith, D., & Defrees, D. J. 1987, ApJ, 312, 351
Hogerheijde, M. R., Jansen, D. J., & van Dishoeck, E. F. 1995, A&A, 294, 792
Huntress, W. T. 1977, ApJS, 33, 495
Jacq, T., Henkel, C., Walmsley, C. M., Jewell, P. R., & Baudry, A. 1988, A&A, 199, L5
Jansen, D. J., Spaans, M., Hogerheijde, M. R., & van Dishoeck, E. F. 1995, A&A, 303, 541
Klein, B., Philipp, S. D., Krämer, I., et al. 2006, A&A, 454, L29
Kruegel, E., & Walmsley, C. M. 1984, A&A, 130, 5
Leurini, S., Schilke, P., Menten, K. M., et al. 2004, A&A, 422, 573
Leurini, S., Rolffs, R., Thorwirth, S., et al. 2006, A&A, 454, L47
Leurini, S., Schilke, P., Wyrowski, F., & Menten, K. M. 2007, A&A, 466, 215
Leurini, S., Parise, B., Schilke, P., Pety, J., & Rolffs, R. 2009, A&A, subm.
Linsky, J. L. 2003, Space Sci. Rev., 106, 49
Lique, F., Toboła, R., Kłos, J., et al. 2008, A&A, 478, 567
Lis, D. C., & Schilke, P. 2003, ApJ, 597, L145
Lis, D. C., Roueff, E., Gérin, M., et al. 2002, ApJ, 571, L55
Maret, S., Ceccarelli, C., Tielens, A. G. G. M., et al. 2005, A&A, 442, 527
Maret, S., Faure, A., Scifoni, E., & Wiesenfeld, L. 2009, ArXiv e-prints
Menten, K. M., Reid, M. J., Forbrich, J., & Brunthaler, A. 2007, A&A, 474, 515
Molek, C., McLain, J., Poterya, V., & Adams, N. G. 2007, J. Phys. Chem. A, 111, 6760
Müller, H. S. P., Thorwirth, S., Roth, D. A., & Winnewisser, G. 2001, A&A, 370, L49
Müller, H. S. P., Schlöder, F., Stutzki, J., & Winnewisser, G. 2005, J. Mol. Struct., 742, 215
Ossenkopf, V. & Henning, T. 1994, A&A, 291, 943
Pagani, L., Vastel, C., Hugo, E., et al. 2009, A&A, 494, 623
Parise, B., Ceccarelli, C., Tielens, A. G. G. M., et al. 2002, A&A, 393, L49
Parise, B., Castets, A., Herbst, E., et al. 2004, A&A, 416, 159
Parise, B., Caux, E., Castets, A., et al. 2005, A&A, 431, 547
Parise, B., Ceccarelli, C., Tielens, A. G. G. M., et al. 2006, A&A, 453, 949
Pety, J., Goicoechea, J. R., Hily-Blant, P., Gerin, M., & Teyssier, D. 2007, A&A, 464, L41
Phillips, T. R., Maluendes, S., & Green, S. 1996, ApJS, 107, 467
Pottage, J. T., Flower, D. R., & Davis, S. L. 2002, J. Phys. B Atom. Mol. Phys., 35, 2541
Pottage, J. T., Flower, D. R., & Davis, S. L. 2004, J. Phys. B Atom. Mol. Phys., 37, 165
Prialnik, D. 2006, in Asteroids, Comets, Meteors, ed. L. Daniela, M. Sylvio Ferraz, & F. J. Angel, IAU Symp., 229, 153
Risacher, C., Vassilev, V., Monje, R., et al. 2006, A&A, 454, L17
Roberts, H., Herbst, E., & Millar, T. J. 2003, ApJ, 591, L41
Roueff, E., Parise, B., & Herbst, E. 2007, A&A, 464, 245
Schilke, P., Walmsley, C. M., Pineau des Forêts, G., et al. 1992, A&A, 256, 595
Schilke, P., Pineau des Forêts, G., Walmsley, C. M., & Martín-Pintado, J. 2001, A&A, 372, 291
Smith, D., Adams, N. G., & Alge, E. 1982, J. Chem. Phys., 77, 1261
Smith, I. W. M., Herbst, E., & Chang, Q. 2004, MNRAS, 350, 323
Turner, B. E. 2001, ApJS, 136, 579
van der Tak, F. F. S., Schilke, P., Müller, H. S. P., et al. 2002, A&A, 388, L53
Walmsley, C. M., Flower, D. R., & Pineau des Forêts, G. 2004, A&A, 418, 1035
Wernli, M., & Faure, A. 2009, MNRAS, in prep
Wernli, M., Valiron, P., Faure, A., et al. 2006, A&A, 446, 367
Wernli, M., Wiesenfeld, L., Faure, A., & Valiron, P. 2007, A&A, 464, 1147
Wilson, T. L. 1999, Reports of Progress in Physics, 62, 143
Xu, L.-H., & Lovas, F. L. 1997, J. Phys. Chem. Ref. Data, 26, 17
Young Owl, R. C., Meixner, M. M., Wolfire, M., Tielens, A. G. G. M., & Tauber, J. 2000, ApJ, 540, 886